RESEARCH ARTICLE

INTERNATIONAL RESEARCH JOURNAL OF MULTIDISCIPLINARY TECHNOVATION

Asian Research Association

DOI: 10.54392/irjmt2353

Exploration on the Structural, Optical, Morphological and Magnetic Properties of Hematite Nanoparticles and Their Antibacterial Activity

P. Rajapandi [a], G. Viruthagiri [a,*]

[a] Department of Physics, Annamalai University, Annamalai Nagar, Chidambaram-608002, Tamil Nadu, India.

*Corresponding Author Email: gvgiri2002@gmail.com

DOI: https://doi.org/10.54392/irjmt2353

Received: 07-08-2023; Revised: 04-09-2023; Accepted: 20-09-2023; Published: 30-09-2023

Abstract: Hematite (α-Fe_2O_3) nanoparticles have been prepared by the conventional chemical precipitation synthesis technique. The prepared samples were subjected to structural, morphological, optical, magnetic and antibacterial behaviours. The diffraction analysis implies that the measured crystallite size of α- Fe_2O_3 nanoparticles is found to be 39 nm. The UV-visible absorption spectroscopy exhibits a strong absorption around 560 nm which is characteristics of Fe_2O_3 nanoparticles and the calculated bandgap value is found to be 2.07 eV. The presence of iron oxide polymorphs can be demonstrated by displaying phonon modes in Raman spectroscopy. Fourier-transform infrared spectroscopy (FTIR) study is used to identify the existence of functional groups and chemical structure of the synthesised Fe2O3 nanoparticles. Magnetic analysis displays hysteretic behaviour at room temperature with saturation magnetization Ms = 0.0036 emu/gm, the remanent magnetization Mr = 0.000698 emu/gm, and coercivity Hc = –0.27 Oe, respectively. The antibacterial activities of these α-Fe2O3 nanoparticles were investigated on pathogenic bacteria Pseudomonas aeruginosa, Bacillus cereus, Staphylococcus aureus, and E. coli by a zone of inhibition method.

Keywords: α Fe_2O_3 nanoparticles, XRD, SEM, Magnetic properties, Antibacterial activity.

1. Introduction

In a variety of fields, nanotechnology holds considerable potential advantages. Recently, nanomaterials have attracted a lot of focus owing to their properties and potential uses due because their distinctive size and form, making their development and manufacture major areas of investigation in nanotechnology [1, 2]. By creating brand-new approaches to resolving environmental issues, nanomaterials have the potential to enhance the environment. The use of magnetic nanoparticles in various magnetic systems is of great interest because of their distinctive nanoscale characteristics. With a Band gap energy of E_g = 2.1 eV, hematite (Fe_2O_3) is the most stable iron oxide and ecologically acceptable semiconductor [3]. Iron oxide (α–Fe_2O_3), is a trendy and potentially useful substance for use in a variety of systems, including gas sensing, photo-catalysts, Li^+-batteries, Na^+-batteries, magnetic components, supercapacitors, photonic devices, and biomedical materials. [4-11].

α-Fe_2O_3 nanoparticles have been created using several ways these techniques of particle production have been expanded, including solgel, microemulsion, sonochemical, and microwave plasma [12-17]. Nanoparticles' physical and chemical characteristics, such as size uniformity and crystallinity, have been shown to differ depending on their microstructure. However, these processes often demand the use of specialised equipment, high temperatures, and the time-consuming and costly elimination of contaminants. Using inorganic salts as precursors, the chemical coprecipitation technique has been employed to create nano or sub-micro particles in several metal oxides (stable materials) [18]. A variety of factors, such as the synthesis process and circumstances, iron oxide can be formed in many phases, such as α–Fe_2O_3 (hematite), γ–Fe_2O_3 (maghemite), and Fe_3O_4 (magnetite). This chapter concentrates on the initial kind of iron oxide (hematite, (α–Fe_2O_3). Among all, α–Fe_2O_3 is frequently obtained in a stable phase throughout the synthesis executions.

The oxygen atoms in the crystal structure of α–Fe_2O_3 are in a hexagonal close packed configuration, with two out of three octahedral sites occupied by Fe^{3+} ions and no periodical defects [19]. The crystalline structure of maghemite (γ–Fe_2O_3) is similar to that of Fe_3O_4, with key difference being that γ–Fe_2O_3 includes only Fe^{3+} cations and vacancies in their sublattices [20].

The magnetic properties of each arrangement differ due to vacancies and valance states in sublattices [21]. These factors impact the saturation magnetization values for bulk α–Fe_2O_3 (65 emu/gm) and γ–Fe_2O_3 (76 emu/gm) [22]. Meanwhile, compared to γ–Fe_2O_3, α–Fe_2O_3 has extraordinarily high coercivity (Hc > 4000 O_e) [23]. Many researchers have recently created nanoscale iron oxide particles using various techniques such as hydrothermal, solgel, coprecipitation, and microwave [24-27]. The chemical precipitation approach was used to create Fe_2O_3 nanoparticles in this study. X-ray diffraction (XRD), UV-vis diffuse reflectance spectroscopy (DRS), Photoluminescence (PL), Raman spectroscopy, Fourier transform infrared (FTIR), Scanning electron microscopy (SEM), Vibrating sample magnetometer (VSM), and antibacterial effectiveness (Negative and positive controls were utilized) were used to characterise the produced powders. After that, the inhibition zones were measured in mm).

2. Experimental Technique

2.1 Materials

The used precursor materials are iron (III) chloride hexahydrate ($Fe_2Cl_3.6H_2O$) with a grade of 99% (Sigma Aldrich Chemical Co., China), and NH_4OH as a precipitant agent 25-28% (Alaa Eldin Co., China). Ethanol (C_2H_6O) > 99.6% (Tian Jin Fuyu Fine Chemical Co., China) was used for washing.

2.2. Synthesis procedure

A simple chemical precipitation process was used to create pure α–Fe_2O_3 nanoparticles. 0.25M of $FeCl_3{\cdot}6H_2O$ have been dissolved in 150 ml of deionized water and stirred for 1 hour at 800 °C to get α–Fe_2O_3. The precipitating agent was a 50 ml aqueous solution of 2M (NH_4OH). To maintain a PH of 10, a base solution (NH_4OH) was progressively added drop by drop. The reaction that occurred in the vessel has been heated to 800 °C using a stirrer with magnetic pellet for three hours. The precipitate was gathered and spun in a centrifuge at 5000 rpm, after which it was repeatedly cleaned in distilled water with ethanol until getting dried in a hot air oven at 800 °C and calcined for 2 hours in a muffle furnace to harvest pure phase of α-Fe_2O_3.

2.3 Characterization

Powder X-ray diffraction (XRD) measurements on the as-synthesized product were carried out on a Rigaku TTRIII X-ray diffractometer with Cu Kα 1 radiation (λ = 1.5406Å). Data were collected over the 2θ range 20–60°. UV-vis absorption spectra in the wavelength range of 200-800 nm measurements were conducted using a Hitachi-U-2001 spectrometer. Photoluminescence (PL) spectroscopy (Horiba spectrometer, iHR-550: 320 nm) was used to investigate the emission properties of the photocatalysts. Micro-Raman spectra of α-Fe_2O_3 NPs were recorded using Horiba Jobin – Yvon Lab Ram HR Raman spectrometer with 532 nm Argon laser as excitation source in the range of 100-800 cm^{-1}. Fourier Transform Infra-Red (FT-IR) spectra of samples were explored by a NICOLET IR200 FT-IR spectrometer with a range from 4000 to 400 cm^{-1}. The Scanning Electron Microscope (SEM) was collected on scanning electron microscopy (SEM) type KYKY-EM3200, 25KV. The elemental analysis has been studied using the energy dispersive X-ray spectroscopy (EDX, BRUKER, INDIA) analysis to confirm the presence of pure elemental Fe and oxygen with no other impurity peaks. VSM analysis was performed to study the magnetic behaviour of used samples at room temperature available at Central Instrumentation Facility, Pondicherry, India.

2.4 Antibacterial Assay

Petri plates containing 20 ml nutrient agar medium were seeded with 24hr culture of bacterial strains *(E.Coli*- 443, *Bacillus cereus*- 441 ,*Pseudomonas aeruginosa* – 424 and *Staphylococcus aureus*- 902*)* Wells were cut and different concentration of sample Pure(500, 250, 100 and 50 µg/ml)was added. The plates were then incubated at 37°C for 24 hours. The antibacterial activity was assayed by measuring the diameter of the inhibition zone formed around the wells. Gentamicin antibiotic was used as a positive control. The values were calculated using Graph Pad Prism 6.0 software (USA).

3. Results and discussion

3.1 Thermogravimetry Differential Thermal Analysis TG/DTA Analyses

Figure.1 Shows the Thermogravimetry Differential Thermal Analysis TG/DTA thermal response curves of pure α-Fe_2O_3 (0.25M). In a nitrogen atmosphere, thermal analysis using TG/DTA measurements was carried out at a 20 °C/min heating rate. The elimination of adsorbed water is responsible for the first weight reduction (6%) seen in Figure. 1

The degradation of organic substances caused a significant loss (36%) between 260 and 648 °C. The DTA thermal response exhibited sharp endothermic peak around 264 °C, demonstrating organic matter breakdown. The sharpness of the endothermic peak indicates that the material being studied is crystalline and pure. As the temperature rises over the melting point, only modest weight loss is detected.

3.2 X–ray diffraction analysis of α–Fe_2O_3

The crystalline structure and phase purity of the prepared α–Fe_2O_3 nanoparticles have been studied by recording powder XRD with cu kα radiation (λ=1.5405Å) from 20^0–60^0.The XRD of the prepared α–Fe_2O_3 nanoparticles is shown in Figure. 2.

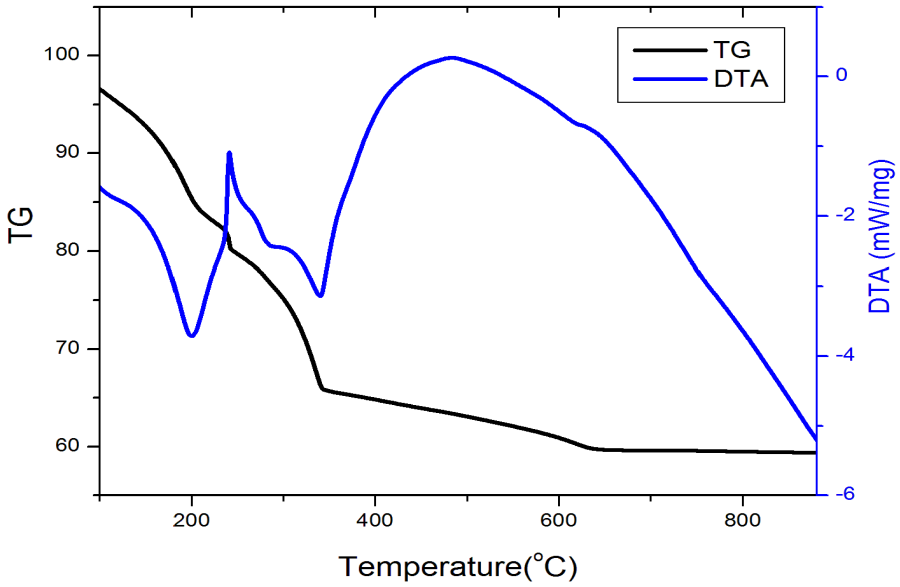

Figure1. Thermogravimetry Differential Thermal Analysis (TG-DTA) patterns of nanosized α-Fe_2O_3

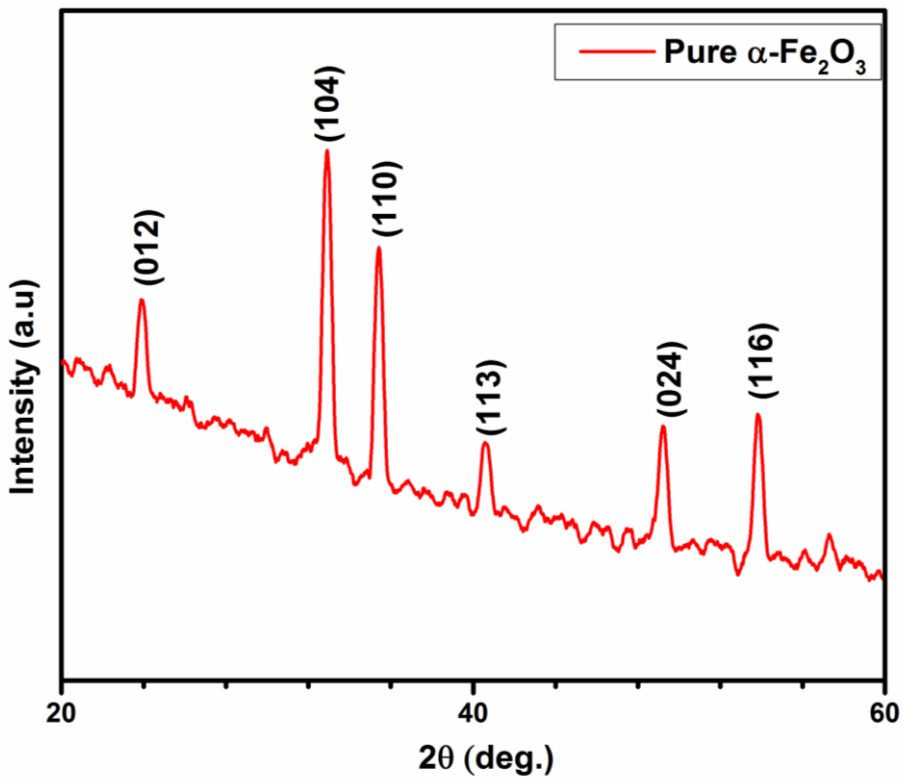

Figure 2. XRD patterns of nanosized α-Fe_2O_3.

All of the diffraction peaks have been identified as having a rhombohedral unit cell and exhibit excellent crystalline nature [JCPDS#89-0598]. Hematite is produced by the Fe_2O_3 transitions from γ – Fe_2O_3 to α–Fe_2O_3. The precise same sample underwent treatment at 400 and 500^0 C (see figure.1 for a thermal characterization of the sample). In the final phase, the composition of Fe_2O_3 with reflection peaks (012), (104), (110), (113), (024), and (116), as well as hematite α-Fe_2O_3, allowed for a reduction in the defect in the Fe_2O_3 nanoparticles and an improvement in the properties of the synthesised nanopowder. The average particle size of the Fe_2O_3 nanoparticles has been calculated using Debye-Scherer's equation, as described by [28, 29].

$$D = 0.9\lambda/\beta cos\theta \quad (1)$$

where, D is grain size of prepared NPs, λ is the wavelength of x-ray, 'β' is a measure of full width at half maximum (FWHM) for the diffraction, M, and θ is the position of the diffraction which determined from the X-ray diffraction pattern (XRD) using the line-width of the typical refraction peaks. These calculated values are used to estimate the dislocation densities. Micro strain occurs as a result of lattice misfit, which varies depending on the deposition conditions (synthesis processes and parameters), and is thus determined using the formula.

$$\varepsilon = \beta cos(\theta/4) \quad (2)$$

The dislocation density (δ) has been calculated with the crystalline size by the formula

$$\delta = 1/D^2 \quad (3)$$

When the annealing temperature was raised from 500 °C to 700 °C, it was also noted that the crystalline size of α–Fe_2O_3 rose from 34 to 44 nm [30]. It can be shown that the predicted size from the XRD measurements is in line with the average crystalline size of bare α–Fe_2O_3, which is 39 nm.

3.3 Diffuse Reflectance Spectral Studies

Iron oxides exhibit a variety of colours as a result of various electronic transitions. The coloured Fe oxides typically have considerable absorption in the ultra violet (UV) and blue spectral regions, but they substantially reflect in the red and infrared. Only a tiny amount of the light beam that strikes the surface of the powdered material is selectively reflected; the other component permeates the sample's bulk and is scattered. Eventually, some of the radiation leaves the bulk and reflects diffusely in all directions. Different iron oxides have been identified and described using the UV-vis diffuse reflectance spectroscopy (UV-DRS) [31].

Figure. 3(a) and Fig. 3(b) depict the diffuse reflectance spectra of prepared Fe_2O_3 nanoparticles in the wavelength region of 200-800 nm. According to Fig. 3(a) and Fig. 3(b), the synthesised nanomaterial exhibits extremely low reflectance between 300 and 575 nm, which is consistent with strong absorption. At roughly 560 nm, reflectance increases sharply. Two faint bands at 240 and 284 nm in the higher energy region are seen, and they are ascribed to metal-ligand charge transfer from, 2p orbital of O to $2E_{2g}$, and $3e_g$ orbitals corresponding the Fe^{3+} [32].

The optical bandgap value (E_g) of the synthesized α–Fe_2O_3 has been calculated using the following expression, and the Taue plot method from the Fig. 3(b).

$$\alpha h\upsilon = (h\upsilon - Eg)^n \quad (4)$$

where, hu is photon energy eV, α is absorption coefficient, cm^{-1}, and n can be ½ (direct allowed), 2 (indirect allowed) depends on the nature of transitions. [33]. An electron can directly emit a photon because electrons in the conduction band acquire comparable momentum as holes in the valence band, which is the process behind the direct and indirect band gaps. A photon has the same energy as the direct bandgap energy. The indirect bandgap in semiconductors arises from the fact that no photon may be released during a transition if an electron undergoes an intermediate state and transfers momentum to the crystal lattice.

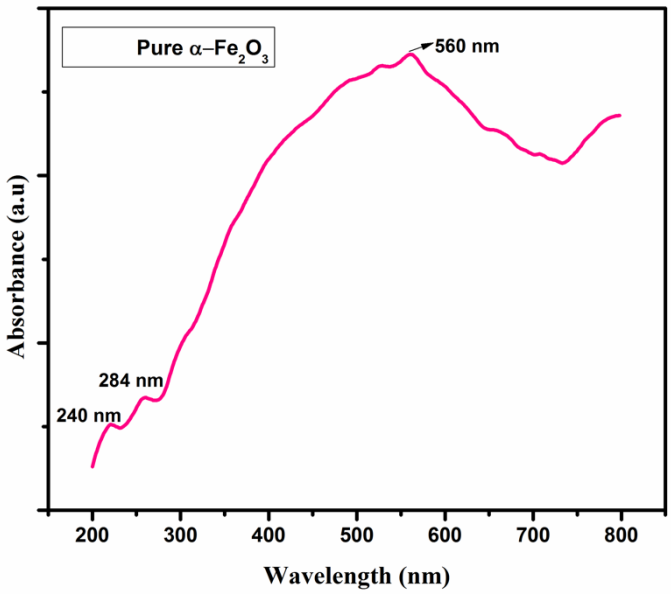

Figure 3 (a). UV-vis diffuse Reflectance Spectrum of α-Fe_2O_3 nanoparticles.

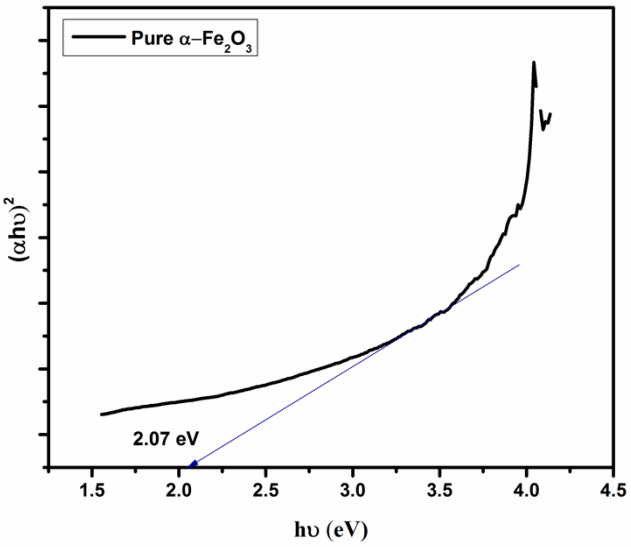

Figure 3(b). Band gap values of the α-Fe_2O_3 nanoparticles

The existing literature on Fe_2O_3 shows indirect bandgaps ranging from 1.38 to 2.09 eV [34-36] and direct bandgaps ranging from 1.95 to 2.35 eV [37-39]. In this study, the measured bandgap value from Tauc's plot of Fig. 3(b) of the prepared Fe_2O_3 was 2.07 eV, indicating that the sample contains an indirect bandgap. Fig. 3 (b) showed a notable red shift as the crystalline size of the nanoparticles increased, which contributed to the spatial confinement effect.

3.4 Photoluminescence study

In the phenomenon of photoluminescence, a material absorbs photons and then emits them again at a different wavelength. This may be described in terms of quantum mechanics as a transition from a lower energy level to a higher energy state, followed by a transition back to the lower energy state and the emission of a photon. Bulk α–Fe_2O_3 lacks photoluminescence owing to forbidden d-d transition, resonant energy migration among dopant and host, an effective lattice, and magnetic relaxation. However, because of the quantum confinement, the α–Fe_2O_3 nanoparticles exhibit luminescence, which causes an electronic state to dislocate and became quantized [40]. Figure (4) depicts the PL spectrum of a material that is stimulated at 480 nm at room temperature. This luminescence can be seen at 484 nm, 538 nm, and 625 nm, with the sample's minimum emission being centred around 484 nm. Furthermore, related emission band around 530 and 625 nm are corresponding to the recombination rate of stimulated charge carriers and oxygen vacancy defects [41]. Three well distinct bands, 484, 530, and 628 nm, exist further in the visible area between 400 and 700 nm (Fig. 4). The electronic transitions of iron vacancies $2D^0 \rightarrow {}^2p$ and $^1D^0 \rightarrow {}^3p$ were identified through emission peaks at 484 nm and 530 nm, respectively. The peak at 625 nm is associated with an oxygen vacancy-related transition of $4p^0 \rightarrow {}^4D$ [42]. According to the literature, the band around 628 nm results of the transition due to ligand field, 530 nm arise from an electron pair transition, and 484 nm from $^6A \rightarrow {}^4E$ transition [43-45]. It was seen from DRS spectra in the wavelength range around 700-800 nm, the absorption observed to be moderate whereas reflectance was strong enough which shows shift to longer wavelength as increase in grain size of NPs. In the current investigation, emission peaks with a lower photo luminescence intensity demonstrated advancement in charge separation efficiency.

3.5 Raman Spectroscopy

The presence of iron oxide polymorphs can be demonstrated by displaying phonon modes in Raman spectroscopy. Different phases of iron oxide exhibit unique Raman peaks, confirming the kind and purity of the synthesised sample's existing phase. Figure. 5 depicts the Raman spectrum of hematite from as prepared nanoparticles calcined at 700 °C. The strong and powerful peaks at 254, 404, 609, and 618 cm^{-1} in the Raman spectrum are the hallmarks of Fe_2O_3; they are associated to E_g phonon mode. Thus data demonstrate that the processed at 700 °C synthesised resultant is α-Fe_2O_3. There was no additional iron oxide (magnetite/maghemite) found, indicating the purity of synthesised α-Fe_2O_3 nanoparticles.

Moreover, comparable findings were reported to explore the Raman spectral vibrations employing with nano α–Fe_2O_3 [46, 47]. Similar results including, A_{1g} and E_g modes in oxygenating α–Fe_2O_3 NPs were reported by Xu *et al.* [47].

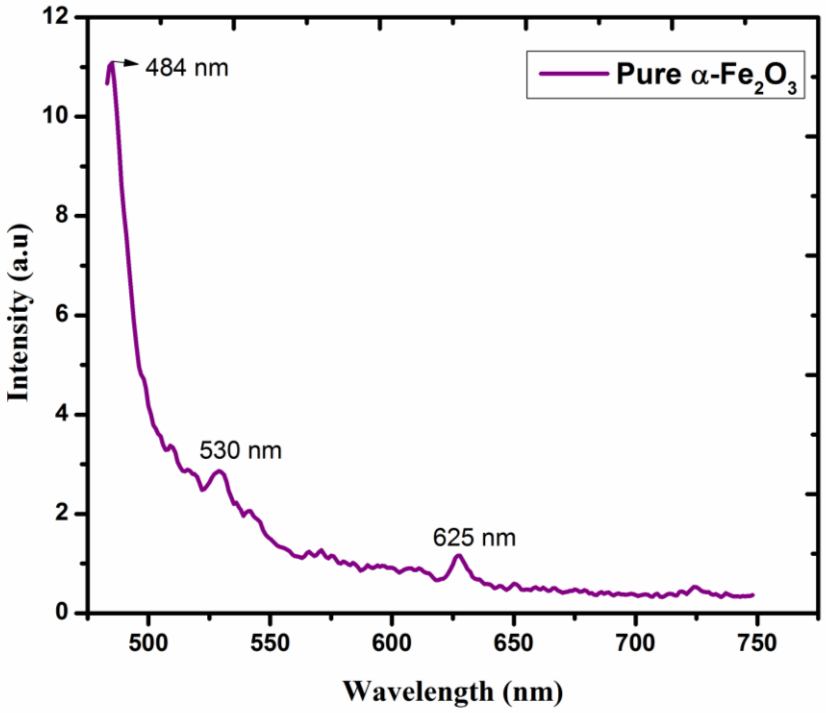

Figure 4. Photo luminescence spectrum of α-Fe2O3 nanoparticles

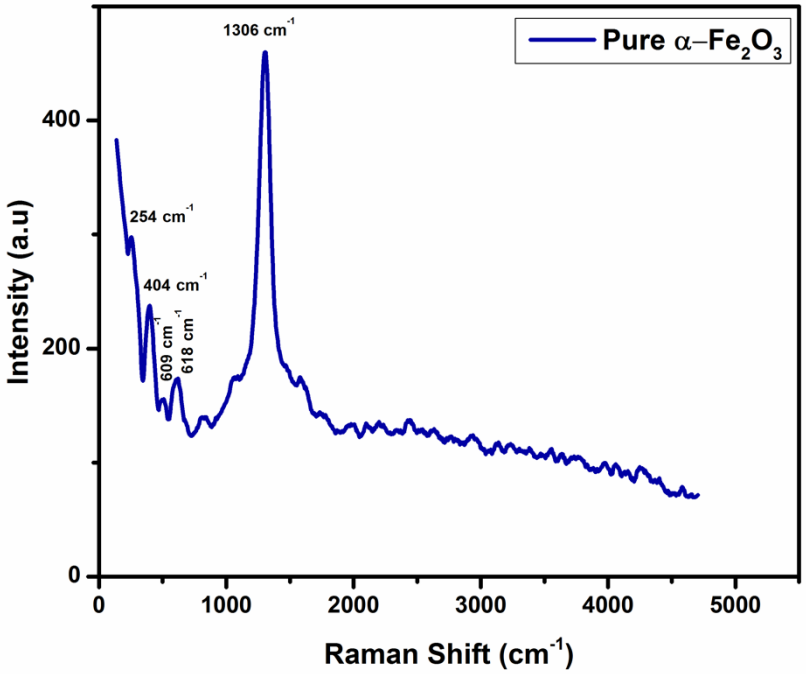

Figure 5. Raman spectrum of α-Fe_2O_3 calcined at 7000c for 2 hours

These results are in agreement with the Raman spectrum of pure Fe_2O_3 crystals with the same rhombohedral structure, which was acquired from the XRD examination of the same sample for the purpose of identifying the crystallinity of synthesised α–Fe_2O_3 calcined at 700 °C.

3.6 Fourier transform infrared spectroscopy (FTIR) Spectral analysis

Fourier transform infrared spectroscopy (FTIR) study is used to identify the existence of functional groups and chemical structure of the synthesised Fe2O3 nanoparticles. Hematite that has been calcined at 700

°C is shown in Fig. 6 as a synthetic product's FT-IR spectrum. The Fe–O band vibration is responsible for the significant IR-absorption band at 555 and 444 cm^{-1} [48, 49]. However, the two bands for the synthesised Fe_2O_3 product that was calcined at 700 °C were at 567 and 473 cm^{-1}, respectively. Fundamental stretching and bending modes vibrations of the hydroxyl (OH^-) groups and/or water molecules (H-O-H) are attributed to the wide absorption band that is centred at 2337 cm^{-1}, 2925 cm^{-1}, 3432 cm^{-1} and should peak around 1630 cm^{-1} [50]. These results are in good accord with the previous values [46, 51–54] and suggest that the broadness of the band may be related to hydrogen bonding between the absorbed water molecules. All of the bonding peaks sharpen and intensify when the powder is calcined at 700 °C, demonstrating the high temperature-induced purity of the nanostructures' crystallinity. The X-ray diffraction (XRD) and Fourier transform-Raman measurements provide strong confirmation of these crystallinity phenomena.

3.7 Morphological investigation

Scanning electron microscopy (SEM) analysis is used to explore the surface morphologies of synthesized sample (calcined at 700 °C), and the findings are shown in Fig. 7 (a) through Fig. 7 (d), for both low and high magnification.

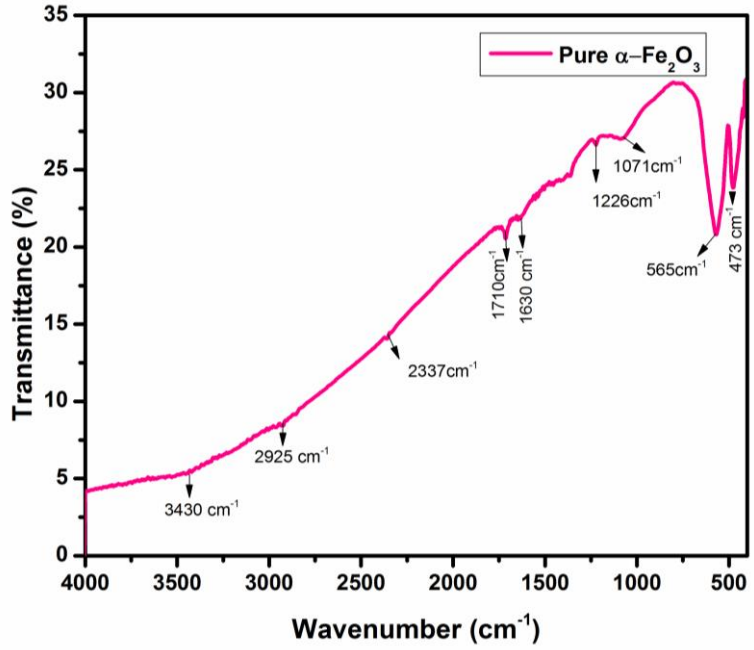

Figure 6. Fourier transform infrared spectrum of α-Fe_2O_3 nanoparticles

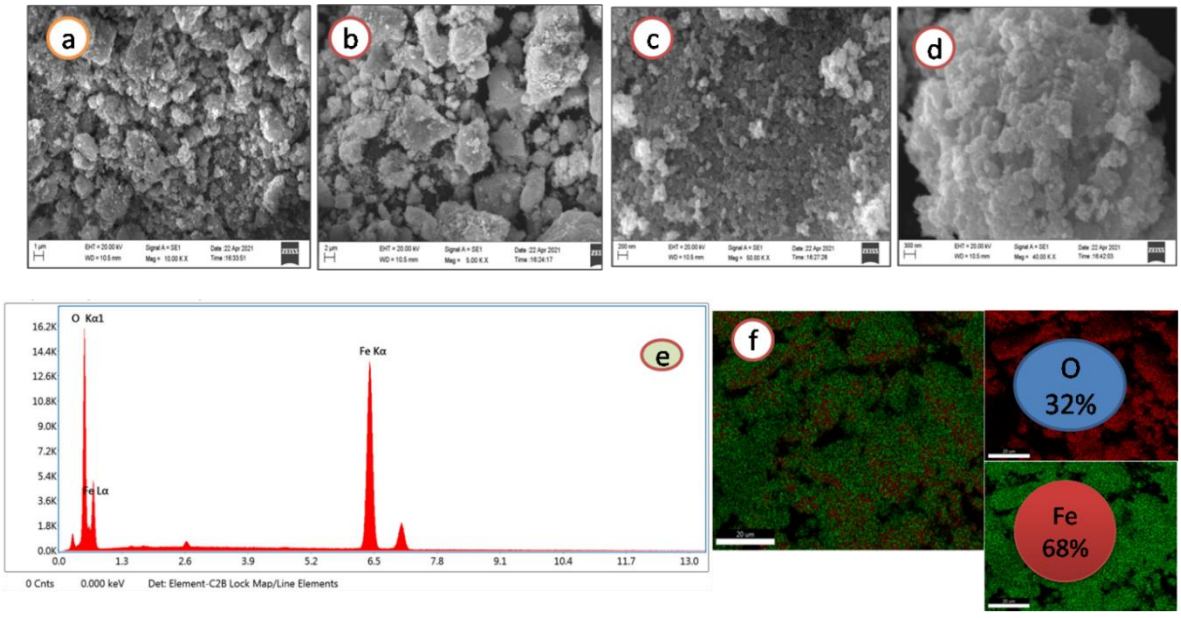

Figure 7. (A-F). SEM images, EDAX spectrum and Elemental mapping of α-Fe_2O_3 nanoparticles

Additionally, a careful examination of the surface morphology photos at high magnification (Fig. 7 (c, d)) revealed that the microspheres were made up of aggregates of spherical nanoparticles with an typical diameter varies from 40 nm to 81 nm (Fig. 7 (a, b)). The ($FeCl_3$, $6H_2O$) precursor aggregation, which produces the hematite nuclei, is the cause of this as the Fe concentration in the aggregation restricts the size of the hematite particles [55]. Figure 7 (e) illustrates the Energy Dispersive Spectroscopy (EDS) examination of Fe_2O_3 nanoparticles, which verifies the presence of iron and oxygen components with respect to weight %. The chemical (elemental) makeup of the material under Scanning electron microscopy (SEM) was examined using the Energy Dispersive Spectroscopy (EDS). If the Fe_2O_3 product is just made up of the elements Fe (68 %) and O (32 %), the Energy Dispersive Spectroscopy (EDS) findings indicated peaks of iron and oxygen (Fig. 7 (e)). The elemental mapping pictures in Fig. 7 (f) illustrate the good spatial distribution of elements in Fe and O. In general, Fe elements are most evenly distributed throughout the whole surface and are in accordance with the elemental mapping.

3.8 Magnetic study

Magnetism is caused by the spatial arrangement (orbital/spin motion) of electrical currents. [51]. It is applied to describe the various magnetic material phases. Only oxygen, chromium, iron, manganese, cobalt, nickel, and several rare earth elements exhibit magnetic ordering in the polyatomic state, while the majority of chemical elements carry an atomic moment in the atomic ground state [52]. The unpaired electrons in each atom's atomic shell, particularly in the 3d and 4f shells are thought to be the primary source of magnetic moments, which are the fundamental component of material magnetism [53].

Thus, magnetic ordering may be produced by the magnetic moment of delocalized electrons in metals and the interatomic interaction between localised magnetic moments in molecules.

The magnetic moment of an atom is produced via interactions involving orbital motion and spin component of electrons, with the latter contributing very little [54]. High spin Fe^{3+} with five unpaired electrons exhibits magnetic moments that are 5.9 Bohr magnetrons in both computations and observations due to its zero orbital moment. The measured magnetic moment of Fe^{2+} (5.1 to 5.5 Bohr magnetrons) varies from the anticipated value (4.9 Bohr magnetrons), showing a contribution from the orbital moment [56]. Pure metals like Fe, Co, and Ni often have the greatest magnetization saturation values, but their severe toxicity and sensitivity to oxidation render them of little use [57]. Iron oxides can therefore offer a consistent magnetic response and are less likely to oxidation.

In general, grain size and surface effect are greatly affecting the magnetic characteristics of nanoparticles [52]. Surface morphological effects are connected to the symmetry infringement of the crystallinity at each particle's periphery, whereas finite size effects are the outcome of the quantum confinement of electrons. Lu *et al*. [58] have covered more in-depth topics. Below a certain particle size, a particle would only have one magnetic domain. The total uncompensated spins in a nanoparticle add up to form a single domain particle's net magnetic moment [59]. Due to the manifestation of super paramagnetic characteristics, particles in the nano-range invariably fall into a single domain. Further, the super paramagnetic properties were observed for α–Fe_2O_3, γ–Fe_2O_3, and Fe_3O_4 with diameters smaller than 20 nm [43], 10 nm and 6 nm [44], respectively.

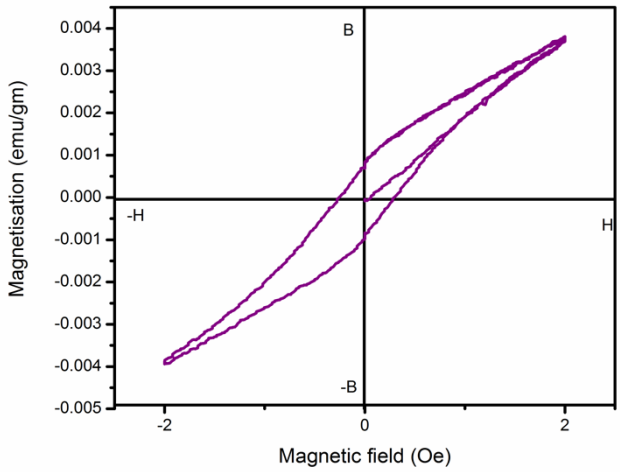

Figure 8. Magnetization versus magnetic field (M-H) plots at room temperature of α-Fe_2O_3 nanoparticles

To obtain saturation magnetization (M_s), magnetic particle magnetization directions must line up with magnetic field directions. Fig. 8 shows the MH curve associated with magnetization for applied magnetic field for the synthesised α–Fe_2O_3 NPs obtained at RT using VSM instrumentation technique. The value of M_s per gram of hematite is 0.0036 emu/g, and the remanent magnetization (M_r) per gram is 0.000698 emu/g; also, the calculated coercivity (Hc) value was found to be –0.27 O_e. A small hysteresis loop and strong coercivity values from the hematite sample contributed to the particle's identification. These findings show that α–Fe_2O_3 hematite nanoparticles have slight ferromagnetic characteristic at ambient condition. Ferromagnetism is the fundamental process that occurs when certain iron magnetic materials, convert into permanent magnets [60]. This was also supported by the X-ray diffraction (XRD) measurements.

3.9 Antibacterial activities

The zone of inhibition approach was used to investigate the antibacterial activity of α–Fe_2O_3 nanoparticles against diverse harmful bacteria, including *Staphylococcus aureus*, *Bacillus cereus*, *Pseudomonas aeruginosa*, and *E. coli*. On a vernier calliper, the zone of inhibition was measured in millimetres (Figure. 9 (a-d)).

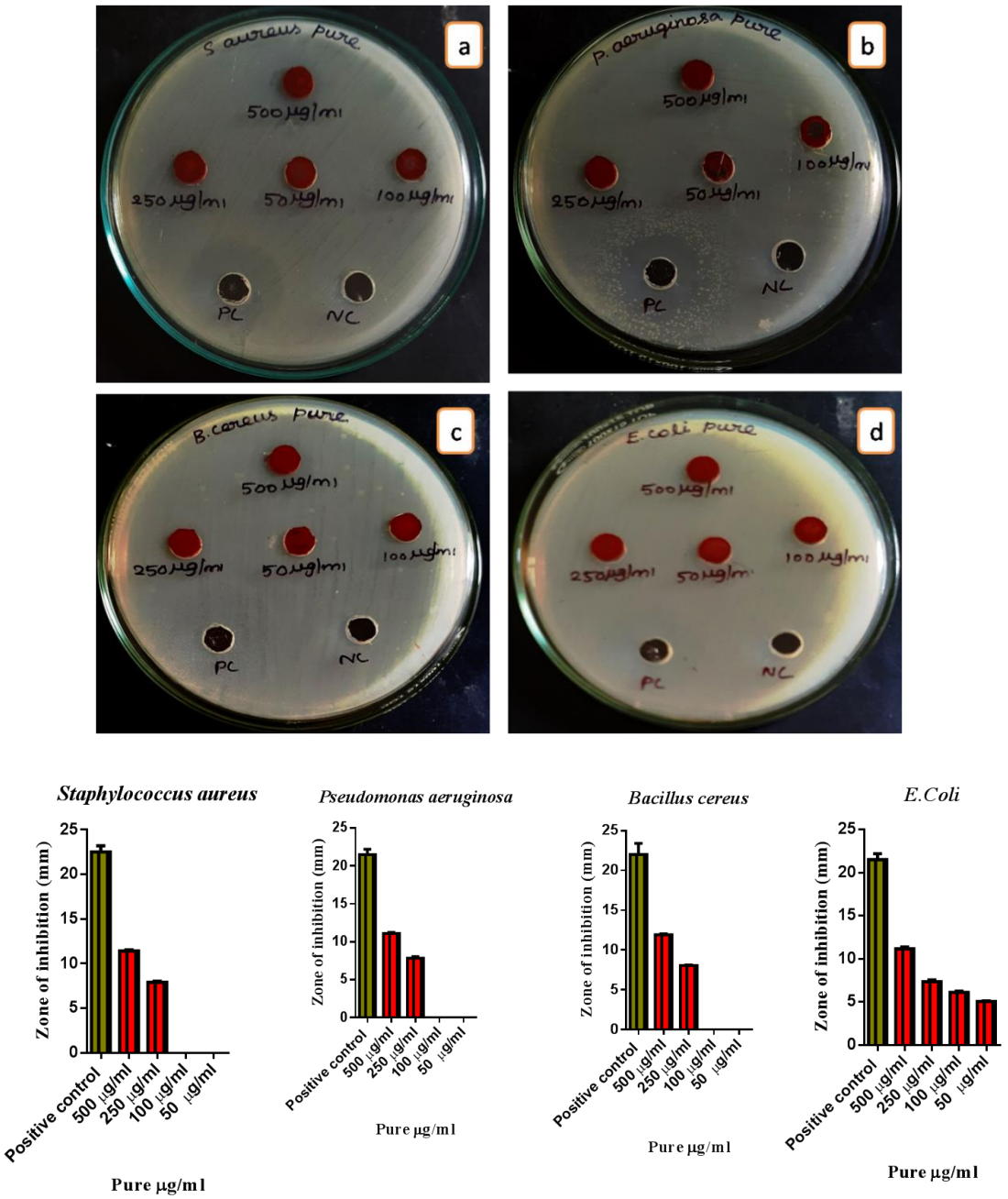

Figure 9. Zone of inhibition of pure α-Fe_2O_3 nanoparticles (a) Staphylococus aureus (b) Pseudomomonas aeruginosa (c) Bacillus cereus and (d) Escherichia coli.

Table 1. Antibacterial activity of α-Fe_2O_3 nanoparticles

S.NO	Name of the test organism	Name of the test sample	Zone of inhibition(mm) SD ± Mean				
			500 µg/ml	250 µg/ml	100 µg/ml	50 µg/ml	Positive control
1.	*Staphylococcus aureus*	Pure (αFe_2O_3)	11.5±0.2	8±0.2	0	0	23±1.0
2.	*E.Coli*		11.3±0.3	7.5±0.3	6.2±0.2	5.1±0.1	22±1.0
3.	*Pseudomonas aeruginosa*		11.2±0.2	8±0.3	0	0	22±1.0
4.	*Bacillus cereus*		12±0.2	8.1±0.1	0	0	23±2.0

The agar plates were infected with hematite nanoparticles at concentrations of 50, 100, 250, and 500 g/ml at the centre well with a diameter of 6 mm. These plates were incubated for 24 hours at room temperature (≈35°C). To get concurrent values (results), all tests were performed in triplicate, and the standard deviation was tabulated (Table 1).

The presence of an inhibition zone in the current investigation suggests that nanoparticles are acting biocidally, maybe via breaking the bacterial membrane. The duration of bacterial suppression is determined by the quantities of nanoparticles as well as the starting bacterial concentration. The smaller the particle size, the greater the membrane permeability and cell death [62]. As a consequence of the nanoparticles enormous surface area i.e. higher surface to volume ratio, they may be firmly adsorbed to the surface of bacterial cells. As a result, they rupture the membrane, allowing internal components to flow out and kill the bacterial cells [63]. Smaller particles with a large surface contact area have a greater bacterial impact than bigger ones [64]. In the present study, nanoparticle concentration was a major factor in their antibacterial activity. In addition to the prior studies, we also propose the potential antibacterial nature of α–Fe_2O_3 nanoparticles which can be further explored for diverse applications.

4. Conclusion

In this study, the sample chemical precipitation synthesis technique was effectively used to prepare α-Fe_2O_3 nanopowders utilising ferric chloride hexahydrate as a precursor. It is concluded from the X-ray diffraction (XRD) pattern, pure nano α-Fe_2O_3 with a rhombohedral structure with grain size of 39 nm were identified. Results from SEM reveal not just particle sizes but also changes in morphology, size distribution, and agglomerations. In addition, in contrast to past research, the precursor nature was discovered to be the primary factor impacting both size and shape. The existence of Fe–O stretching mode of α–Fe_2O_3 was detected in the Fourier transform infrared (FTIR) spectra. The four phonon modes of the rhombohedral product are seen in the raman spectrum, which also depicts the development of the crystal formations. Energy dispersive spectral (EDS) analysis shows merely peaks of Fe and oxygen, proving that the absence of impurities in prepared hematite nanoparticles. With an optical band gap of roughly 2.07 eV, the UV-vis absorption of α-Fe_2O_3 nanoparticles revealed a high peak at 240, 284, and 560 nm. The magnetic characteristics of the α–Fe_2O_3 nanoparticles were examined. The relationship between the particle size and various preparation factors has been researched and rationally explained, as well as the relationship between the coercivities and the magnetic moment and size. On both gram-positive and gram-negative bacterial strains, the α–Fe_2O_3 nanoparticles demonstrated their antibacterial properties. We may infer that α–Fe_2O_3 is a highly potent antibacterial agent given the size of the zone of inhibition.

References

[1] K. Lu, Nanocrystalline metals crystallized from amorphous solids: nanocrystallization, structure, and properties, Materials Science and Engineering: R: Reports, 16(4), (1996) 161-221. https://doi.org/10.1016/0927-796X(95)00187-5

[2] Z. Wu, S. Yang, W. Wu, Shape control of inorganic nanoparticles from solution, Nanoscale, 8, (2016) 1237-1259. https://doi.org/10.1039/C5NR07681A

[3] D. Cao, P. He, N. Hu, Electrochemical biosensors utilising electron transfer in heme proteins immobilised on Fe_3O_4 nanoparticles,

Analyst, 128(10), (2003) 1268-1274. https://doi.org/10.1039/B308242C

[4] S. Agarwala, Z.L. Lim, E. Nicholson, G.W. Ho, Probing the morphology-device relation of Fe2O3nanostructures towards photovoltaic and sensing applications. Nanoscale, 4 (2012) 194-205. https://doi.org/10.1039/C1NR10856E

[5] W. Wu, R. Hao, F. Liu, X. Su, Y. Hou, Single-crystalline α-Fe 2 O 3 nanostructures: controlled synthesis and high-index plane-enhanced photodegradation by visible light. Journal of Materials Chemistry A, 23 (2013) 6888-6894. https://doi.org/10.1039/C3TA10886D

[6] Yan. Zhao, Y. Liu, H. Liu, H. Kang, K. Cao, Q. Wang, C. Zhang, Y.Wang, H. Yuan, L. Jiao, Improved dehydrogenation performance of LiBH4 by 3D hierarchical flower-like MoS2 spheres additives. Journal of Power Sources, 300 (2015) 358-364. https://doi.org/10.1016/j.jpowsour.2015.09.088

[7] M. Fiore, G. Longoni, S. Santangelo, F. Pantò, S. Stelitano, P. Frontera, P. Antonucci, R. Ruffo, Electrochemical characterization of highly abundant, low cost iron (III) oxide as anode material for sodium-ion rechargeable batteries. Electrochimica Acta, 269 (2018) 367-377. https://doi.org/10.1016/j.electacta.2018.02.161

[8] J. Ma, J. Lian, X. Duan, X. Liu, W. Zheng. α-Fe_2O_3: hydrothermal synthesis, magnetic and electrochemical properties. The Journal of Physical Chemistry C, 114(24), (2010) 10671-10676. https://doi.org/10.1021/jp102243g

[9] V.D. Nithya, N. Sabari Arul, Review on α-Fe_2O_3 based negative electrode for high performance supercapacitors. Journal of Power Sources, 327 (2016) 297-318. https://doi.org/10.1016/j.jpowsour.2016.07.033

[10] C.P. Singh, K.S. Bindra, G.M. Bhalerao, S.M. Oak. Investigation of optical limiting in iron oxide nanoparticles. Optics Express, 16(12), (2008) 8440-8450. https://doi.org/10.1364/OE.16.008440

[11] W. Wu, C.Z. Jiang, V.A. Roy, Designed synthesis and surface engineering strategies of magnetic iron oxide nanoparticles for biomedical applications. Nanoscale, 8(47), (2016) 19421-19474. https://doi.org/10.1039/C6NR07542H

[12] J. Chen, L. Xu, W. Li, X. Gou, α-Fe_2O_3 nanotubes in gas sensor and lithium-ion battery applications. Advanced Materials, 17(5), (2005) 582-586. https://doi.org/10.1002/adma.200401101

[13] X. Wen, S. Wang, Y. Ding, Z.L. Wang, S. Yang, Controlled growth of large-area, uniform, vertically aligned arrays of α-Fe2O3 nanobelts and nanowires. The Journal of Physical Chemistry B, 109(1), (2005) 215-220. https://doi.org/10.1021/jp0461448

[14] K. Woo, H.J. Lee, J-P. Ahn, Yong Sung Park. Sol–gel mediated synthesis of Fe2O3 nanorods. Advanced Materials, 15(20), (2003) 1761-1764. https://doi.org/10.1002/adma.200305561

[15] H. Xu, L. Cui, N. Tong, H. Gu, Development of high magnetization Fe_3O_4/polystyrene/silica nanospheres via combined miniemulsion/emulsion polymerization. Journal of the American Chemical Society, 128(49), (2006) 15582-15583. https://doi.org/10.1021/ja066165a

[16] R. Vijayakumar, Y. Koltypin, I. Felner, A. Gedanken, Sonochemical synthesis and characterization of pure nanometer-sized Fe_3O_4 particles. Materials Science and Engineering A, 286(1), (2000) 101-105. https://doi.org/10.1016/S0921-5093(00)00647-X

[17] S-Z. Li, Y.C. Hong, Han S. Uhm, Zhe-Kui Li. Synthesis of nanocrystalline iron oxide particles by microwave plasma jet at atmospheric pressure. Japanese journal of applied physics, 43(11R) (2004) 7714. https://doi.org/10.1143/JJAP.43.7714

[18] R.T. Rasheed, S.D. Al-Algawi, H.H. Kareem, H.S. Mansoor. Preparation and characterization of hematite iron oxide (α-Fe2O3) by sol-gel method, Chemical sciences journal, 9(4), (2018) 1000197. https://doi.org/10.4172/2150-3494.1000197

[19] W. Szymański, M. Skiba, A. Błachowski. Mineralogy of Fe–Mn nodules in albeluvisols in the Carpathian Foothills, Poland. Geoderma, 217 (2014) 102-110. https://doi.org/10.1016/j.geoderma.2013.11.008

[20] S. Alibeigi, M.R. Vaezi, Phase transformation of iron oxide nanoparticles by varying the molar ratio of Fe2+: Fe3+. Chemical Engineering & Technology: Industrial Chemistry-Plant Equipment-Process Engineering-Biotechnology, 31(11), (2008) 1591-1596. https://doi.org/10.1002/ceat.200800093

[21] M.M. Can, M. Coşkun, T. Fırat, A comparative study of nanosized iron oxide particles; magnetite (Fe3O4), maghemite (γ-Fe2O3) and hematite (α-Fe2O3), using ferromagnetic resonance. Journal of Alloys and Compounds, 542 (2012) 241-247. https://doi.org/10.1016/j.jallcom.2012.07.091

[22] Z. Jia, J. Liu, Q. Wang, S. Li, Q. Qi, R. Zhu, Synthesis of 3D hierarchical porous iron oxides for adsorption of Congo red from dye wastewater. Journal of Alloys and Compounds, 622 (2015) 587-595. https://doi.org/10.1016/j.jallcom.2014.10.125

[23] M. Tadic, N. Citakovic, M. Panjan, B. Stanojevic, D. Markovic, Đ. Jovanovic, V. Spasojevic, Synthesis, morphology and microstructure of pomegranate-like hematite (α-Fe2O3) superstructure with high coercivity. Journal of Alloys and Compounds, 543, (2012) 118-124. https://doi.org/10.1016/j.jallcom.2012.07.047

[24] X. Zhang, Y. Niu, Y. Li, X. Hou, Y. Wang, R. Bai, J. Zhao, Synthesis, optical and magnetic properties of α-Fe2O3 nanoparticles with various shapes. Materials letters, 99 (2013) 111-114. https://doi.org/10.1016/j.matlet.2013.02.070

[25] F.N. Sayed, V. Polshettiwar, Facile and sustainable synthesis of shaped iron oxide nanoparticles: effect of iron precursor salts on the shapes of iron oxides. Scientific reports, 5(1) (2015) 9733. https://doi.org/10.1038/srep09733

[26] G. Kandasamy, D. Maity, Recent advances in superparamagnetic iron oxide nanoparticles (SPIONs) for in vitro and in vivo cancer nanotheranostics. International journal of pharmaceutics, 496(2), (2015) 191-218. https://doi.org/10.1016/j.ijpharm.2015.10.058

[27] S. Shi, J-Y. Hwang, Microwave-assisted wet chemical synthesis: advantages, significance, and steps to industrialization. Journal of Minerals and Materials Characterization and Engineering, 2(2), (2003) 101-110. https://doi.org/10.4236/jmmce.2003.22009

[28] R.M. Cornel, U. Schwertmann, (1996). the iron oxides. Structure, properties, reactions and uses. Wiley-VCH GmbH, Germany.

[29] R.T. Rasheed, S.D. Al-Algawi, Annealing effect of SnO_2 nanoparticles prepared by the sol–gel method. Journal of Advanced Physics, 5(3), (2016) 236-240. https://doi.org/10.1166/jap.2016.1262

[30] P. Mallick, B.N. Dash, X-ray diffraction and UV-visible characterizations of α-Fe_2O_3 nanoparticles annealed at different temperature. Nanoscience and Nanotechnology, 3(5), (2013) 130-134.

[31] J. Torrent, V. Barrón, Diffuse reflectance spectroscopy of iron oxides. Encyclopedia of surface and Colloid Science, 1 (2002) 1438-1446.

[32] J. Wang, W.B. White, J.H. Adair, Optical properties of hydrothermally synthesized hematite particulate pigments. Journal of the american Ceramic Society, 88(12), (2005) 3449-3454. https://doi.org/10.1111/j.1551-2916.2005.00643.x

[33] B.K. Pandey, A.K. Shahi, J.R.K. Kotnala, R. Gopal, Optical and magnetic properties of Fe_2O_3 nanoparticles synthesized by laser ablation/fragmentation technique in different liquid media. Applied Surface Science, 289 (2014) 462-471. https://doi.org/10.1016/j.apsusc.2013.11.009

[34] L. Dghoughi, B. Elidrissi. C. Berne de, M. Addou, M.A. Lamrani, M. Regragui, H. Erguig, Physico-chemical, optical and electrochemical properties of iron oxide thin films prepared by spray pyrolysis. Applied Surface Science, 253(4), (2006) 1823-1829. https://doi.org/10.1016/j.apsusc.2006.03.021

[35] N. Beermann, L. Vayssieres, S-E. Lindquist, A. Hagfeldt, Photo electrochemical studies of oriented nanorod thin films of hematite. Journal of the Electrochemical Society, 147(7) (2000) 2456. https://doi.org/10.1149/1.1393553

[36] N. Ozer, F. Tepehan. Optical and electrochemical characteristics of sol–gel deposited iron oxide films. Solar Energy Materials and Solar Cells, 56(2), (1999) 141-152. https://doi.org/10.1016/S0927-0248(98)00152-4

[37] M. Tang, B. Sun, J. Huang, J. Gao, C. Ming Li. High performance white-light-controlled resistance switching memory of an Ag/α-Fe_2O_3/FTO thin film. Rsc Advances, 6(30) (2016) 25028-25033. https://doi.org/10.1039/C5RA24057C

[38] M. Gartner, M. Crisan, A. Jitianu, R. Scurtu, R. Gavrila, I. Opera, M. Zaharescu, Spectroellipsometric Characterization of Multilayer Sol-Gel Fe_2O_3 Films. Journal of Sol-Gel Science and Technology, 26 (2003) 745-748. https://doi.org/10.1023/A:1020706423230

[39] R.N. Goyal, A.K. Pandey, D. Kaur, A. Kumar, Fabrication of α-Fe_2O_3 nanopowder modified glassy carbon electrode for applications in electrochemical sensing. Journal of nanoscience and nanotechnology, 9(8) (2009) 4692-4699. https://doi.org/10.1166/jnn.2009.1278

[40] P. Shikha, B.S. Randhawa, T.S. Kang, Greener synthetic route for superparamagnetic and luminescent α-Fe_2O_3 nanoparticles in binary mixtures of ionic liquid and ethylene glycol. RSC

Advances, 5(63), (2015) 51158-51168. https://doi.org/10.1039/C5RA07218B

[41] L. El Mir, Luminescence properties of calcium doped zinc oxide nanoparticles. Journal of Luminescence, 186 (2017) 98-102. https://doi.org/10.1016/j.jlumin.2017.02.029

[42] P. Thomas, K.E. Abraham, Synthesis of Iron Oxide Nanoparticles and Study of Its Opticalproperties. SB Academic Review, (2012) 108-116

[43] G-Y. Zhang, YY. Xu, D-Z. Gao, Y-Q Sun, α-Fe_2O_3 nanoplates: PEG-600 assisted hydrothermal synthesis and formation mechanism. Journal of alloys and compounds, 509(3), (2011) 885-890. https://doi.org/10.1016/j.jallcom.2010.09.124

[44] L. Lu, L. Li, X. Wang, G. Li, Understanding of the finite size effects on lattice vibrations and electronic transitions of nano α-Fe_2O_3. The Journal of Physical Chemistry B, 109(36), (2005) 17151-17156. https://doi.org/10.1021/jp052780

[45] Y. Yamanoi, S. Nakashima, M. Katsura, Temperature dependence of reflectance spectra and color values of hematite by in situ, high-temperature visible micro-spectroscopy. American Mineralogist, 94(1), (2009) 90-97. https://doi.org/10.2138/am.2009.2779

[46] A. Lassoued, B. Dkhil, A. Gadri, S. Ammar, Control of the shape and size of iron oxide (α-Fe_2O_3) nanoparticles synthesized through the chemical precipitation method. *Results in physics*, 7 (2017) 3007-3015. https://doi.org/10.1016/j.rinp.2017.07.066

[47] Y.Y. Xu, D. Zhao, X.J. Zhang, W.T. Jin, P. Kashkarov, H. Zhang, Synthesis and characterization of single-crystalline α-Fe2O3 nanoleaves. Physica E: Low-dimensional Systems and Nanostructures, 41(5), (2009) 806-811. https://doi.org/10.1016/j.physe.2008.12.015

[48] H. Liu, P. Li, B. Lu, Y. Wei, Y. Sun, Transformation of ferrihydrite in the presence or absence of trace Fe (II): the effect of preparation procedures of ferrihydrite. Journal of Solid State Chemistry, 182(7), (2009) 1767-1771. https://doi.org/10.1016/j.jssc.2009.03.030

[49] Z. Jing, S. Wu, Synthesis and characterization of monodisperse hematite nanoparticles modified by surfactants via hydrothermal approach. Materials Letters, 58(27-28), (2004) 3637-3640. https://doi.org/10.1016/j.matlet.2004.07.010

[50] E. Darezereshki, One-step synthesis of hematite (α-Fe_2O_3) nano-particles by direct thermal-decomposition of maghemite, Materials Letters, 65(4), (2011) 642-645. https://doi.org/10.1016/j.matlet.2010.11.030

[51] R.D. Ambashta, M. Sillanpa, Water purification using magnetic assistance: a review. Journal of hazardous materials, 180(1-3) (2010) 38-49. https://doi.org/10.1016/j.jhazmat.2010.04.105

[52] Y.A. Koksharov, Magnetism of nanoparticles: effects of size, shape, and interactions. Magnetic nanoparticles, (2009) 197-254. https://doi.org/10.1002/9783527627561.ch6

[53] A. Akbarzadeh, M. Samiei, S.Davaran, Magnetic nanoparticles: preparation, physical properties, and applications in biomedicine. Nanoscale research letters, 7(144), (2012) 1-13. https://doi.org/10.1186/1556-276X-7-144

[54] D. Ramimoghadam, S. Bagheri, S.B.A. Hamid Progress in electrochemical synthesis of magnetic iron oxide nanoparticles. Journal of Magnetism and Magnetic Materials, 368 (2014) 207-229. https://doi.org/10.1016/j.jmmm.2014.05.015

[55] U. Schwertmann, J. Friedl, H. Stanjek, From Fe (III) ions to ferrihydrite and then to hematite. Journal of colloid and interface science, 209(1), (1999) 215-223. https://doi.org/10.1006/jcis.1998.5899

[56] Y.L. Pang, S. Lim, H.C. Ong, W.T. Chong, Research progress on iron oxide-based magnetic materials: synthesis techniques and photocatalytic applications. Ceramics International, 42(1) (2016) 9-34. https://doi.org/10.1016/j.ceramint.2015.08.144

[57] J. Torrent, V. Barrón, Diffuse reflectance spectroscopy of iron oxides. Encyclopedia of surface and Colloid Science, 1 (2002) 1438-1446.

[58] A.H. Lu, E.E. Salabas, F. Schüth, Magnetic nanoparticles: synthesis, protection, functionalization, and application. Angewandte Chemie International Edition, 46(8) (2007) 1222-1244. https://doi.org/10.1002/anie.200602866

[59] S. Shylesh, V. Schünemann, W.R. Thiel, Magnetically separable nanocatalysts: bridges between homogeneous and heterogeneous catalysis. Angewandte Chemie International Edition, 49(20), (2010) 3428-3459. https://doi.org/10.1002/anie.200905684

[60] E. Darezereshki, F. Bakhtiari, M. Alizadeh, A.B. Vakylabad, M. Ranjbar, Direct thermal

decomposition synthesis and characterization of hematite (α-Fe2O3) nanoparticles. Materials Science in Semiconductor Processing, 15(1), (2012) 91-97. https://doi.org/10.1016/j.mssp.2011.09.009

[61] E.N. Taylor, T.J. Webster, The use of superparamagnetic nanoparticles for prosthetic biofilm prevention. International journal of nanomedicine, (2009) 145-152. https://doi.org/10.2147/IJN.S5976

[62] S. Ankanna, N. Savithramma, Biological synthesis of silver nanoparticles by using stem of Shorea tumbuggaia Roxb. and its antimicrobial efficacy. Asian Journal of Pharmaceutical and Clinical Research, 4(2) (2011) 137-141.

[63] L. Qj, Z. Xu, X. Tiang, C. Hu, X. Zou, Preparation and antibacterial activity of chitosan nanoparticles. Carbohydrate Research, 339(16), (2004) 2693-2700. https://doi.org/10.1016/j.carres.2004.09.007

[64] A. Panáček, L. Kvítek, R. Prucek, M. Kolář, R. Večeřová, N. Pizúrová, V.K. Sharma, T. Nevěčná, R. Zbořil, Silver colloid nanoparticles: synthesis, characterization, and their antibacterial activity. The Journal of Physical Chemistry B, 110(33), (2006) 16248-16253. https://doi.org/10.1021/jp063826h

Acknowledgement

We thank the Head, Department of Physics, Annamalai University for providing the necessary facilities and the Principal, Thiru. Kolanjiappar Government Arts College, Viruthachalam. This research did not receive any specific grant from funding agencies in the public, commercial, or not-for-profit sectors.

Has this article screened for similarity?

Yes

Authors Contribution Statement

P. Rajapandi; Conceptualization, Methodology, Validation, Formal analysis, Investigation, Writing - Original Draft, Writing - Review & Editing, G. Viruthagiri; Supervision, Formal analysis, Validation, Resources, Writing - Original Draft, Writing - Review & Editing

Declaration of Competing Interest

The Authors declare that they have no known competing financial interests or personal relationships that could have appeared to influence the work reported in this paper.

Conflict of Interest

The Authors have no conflicts of interest on this article to declare.

About the License